IEEE *Access*

Multidisciplinary : Rapid Review : Open Access Journal

RESEARCH ARTICLE

Analytical and Experimental Investigation of Electromagnetic Tracking System for Location and Orientation Estimation

CHUN-YEON LIN, (Member, IEEE), YI-CHIN WU, (Graduate Student Member, IEEE), ZHONG-HSIANG KUO, HSI-YEN MA, AND MEGAN TENG

Department of Mechanical Engineering, National Taiwan University, Taipei 10617, Taiwan

Corresponding author: Chun-Yeon Lin (chunyeonlin@ntu.edu.tw)

ABSTRACT This paper presents the development of an electromagnetic (EM) tracking system that consists of a pyramid field generator (PFG) of five excitation coils and a sensing coil for location and orientation estimation. The system measures the induced electromotive forces (EMF) of the sensing coil with the change of the magnetic field contributed by the PFG. The proposed modeling distributed magnetic flux (DMF) method that divides the multi-turns sensing coil into multiple layers and concentric circles for the distributed elements is utilized to determine EMF induced in the sensing coils for investigating the effects of translational and angular displacement. The finite element analysis numerically verifies the DMF method and validates the Artificial Neural Network (ANN)-based estimation models. The calibration and ANN-based estimation process are applied to inversely estimate the location and orientation of the sensing coil based on the DMF method and the experimental EM tracking system. The proposed design and a prototype of the EM tracking system have experimentally verified the DMF method and showed the validity of the location and orientation estimation.

INDEX TERMS Electromagnetic tracking, sensing system, location, orientation estimation.

I. INTRODUCTION

In computer-aided medicine, object tracking is a crucial technology that allows accurate positioning of the medical device or where the anatomy is being performed [1]. Compared to the traditional methods, conventional computer-assisted interventions could help improve the accuracy of the surgery and reduce the time of intrusion [2]. For example, image-guided therapy could correct the operation location of a patient by preoperative X-ray computed tomography or intra-operative ultrasound [3]. However, image-guided therapy only provides information regarding the relative location between the equipment and the patient with want accuracy. Hence, the importance of computer-assisted intervention research in three-dimensional space tracking technology

The associate editor coordinating the review of this manuscript and approving it for publication was Siddharth Tallur.

would address the need for better instruments. Optical tracking is the most popular method in the industry, utilizing a camera to locate the optical tag. This method boasts great accuracy, but the difficulty in implementing it in places with insufficient lighting or obscured line of sight suggests some disadvantages to this technology. This problem concerns minimally invasive surgeries, in which flexible endoscopes, catheters, and needle tips enter the body during the operation and can not be tracked or observed easily.

Electromagnetic tracking offers similar functions without the need for visual clarity [1]. This advantage leads to many possibilities in clinical applications, including intra-body navigation of medical instruments during an operation in tissues or internal organs such as the liver [2], lungs [4], spline, kidney, adrenal glands, pancreas, lymph nodes, and pelvis [5], [6], bronchoscopy [7], [8], neurosurgery [9] and ear, nose and throat surgery [10]. Other applications include

IEEE Access

C.-Y. Lin et al.: Analytical and Experimental Investigation of EM Tracking System for Location and Orientation Estimation

measuring the measurement and analysis of kinematics with high degrees of freedom [11], the positioning of objects in virtual reality [12], motion tracking and drill navigation [13], and the location of continuum medical robots [14].

The basic EM tracking device consists of a field generator and an EM sensor. When the field generator is activated, the sensor could pick up the resulting change in the electromagnetic field, which could then be used to position the device [15]. The general procedures are as follows: when the device is placed on top of a sample, the field generator is activated with a specific input waveform. The EM sensor then perceives the magnetic field density (**B**) change that manifests as the magnetic flux (MF) and electromotive force (EMF). The distance between the sample and the device, along with the relative pose of the sensor, is correlated to the measured EMF. With this relationship, the **B** as perceived by the EM sensor, could be used to calculate the exact position and pose of the device inversely.

The common design for the field generator is the triaxial generator design that provides sufficiently unique magnetic fields in three orthogonal directions using three orthogonal coils [16]. A single coaxial transmitter can also achieve six-degree-of-freedom (DoF) tracking without the variability of the orientation [17]. Similar to the field generator, there are several choices in creating sensing agents to pair with the generator. The anisotropic magnetoresistive (AMR) has a compact size and high sensitivity to receive the **B** in the air. The simple structure of the triaxial AMR was utilized to compute six-DoF position tracking with 2.6 ± 0.79mm pose error and 1.4 ± 0.61o orientation error [17]. The three-DoF digital magnetic sensor with array placement is also used to track the three-DoF displacement of three air-core coils with a mean absolute error of 3 mm at 42 cm [18]. The triaxial tunnel magnetoresistance (TMR) sensors are used as anchors to estimate five-DoF information on the excitation coil [19]. However, the position error would emerge in the long-range caused by the measurement constraint for the sensor design. For long-distance and six-DoF measurements in practical applications, the sensing coil could more flexibly adjust the geometry of the coil to meet the actual system.

The common method is using the sensing coil to measure the change of the MF by the varying EMF [1]. The large-area coils, which effectively capture the change in MF in space, are utilized to assist in the calculation of position and roll angle [20]. The quantitative evaluations of some commercial electromagnetic tracking systems have been analyzed [21]. The NDI aurora has a relative error of 0.96mm±0.68mm, and Ascension microBIRD has a relative error of 1.14mm±0.78mm for a distance of 50 mm. The relative rotation errors are $0.51°$ and $0.04°$, respectively. Apart from sensing coils, a fluxgate sensor which constitutes two coils with opposite polarity and measures the second harmonic Fourier component of the magnetic field is designed for measuring the direct current component of the magnetic field, while a sensing coil detects the alternating current fields [12].

The modeling of the magnetic fields is needed to design magnetic sensing devices. In some research, the magnetic flux densities generated from the coils are formulated by the magnetic moment vectors. The closed-form formulas of location and orientation are deduced [12] or solved numerically by a nonlinear least-square optimization algorithm [22]. Apart from the magnetic moment vectors, the magnetic field is modeled characterized by the distributed multipole models for calculating the magnetic field around a permanent magnet or an electromagnet for designing a permanent-magnet-based actuator [23] and magnetic induction tomography [24].

Motivated by the need for a tracking system to estimate the posture and position of the sensing coil bolstered by rigorous theoretical analysis, this paper illustrates an EM tracking system design that fits this description. The remainder of this paper offers the following:
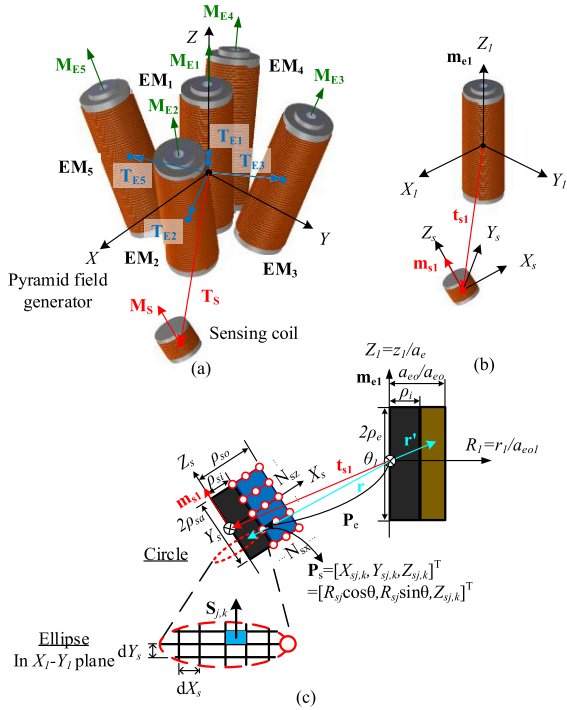
– An EM tracking system design that uses a five-EM-pyramid field generator (PFG) and a sensing coil for the six-DoF tracking is introduced. The induced EMF of the sensing coil is expressed in the closed-form solution by the proposed distributed magnetic flux (DMF) method and through the numerical integration to simplify and discrete the solutions.

– The effects on the sensing coil of the translational and angular displacement by comparing the values of the DMF method with FEA simulations and constructing are verified, and the inverse estimation model for the estimation of location and orientation through the artificial neural network (ANN) is validated.

– The calibration and estimation processes experimentally illustrate the location and orientation estimation feasibility.

II. ELECTROMAGNETIC TRACKING SYSTEM DESIGN

Fig. 1 illustrates the proposed design of an EM tracking system for six-DoF parameters of location $\mathbf{T}_S = [T_{Sx}, T_{Sy}, T_{Sz}]^T$ and orientation $\mathbf{M}_S = [M_{Sx}, M_{Sy}, M_{Sz}]^T$ estimation of the sensing coil. The PFG consists of five identical excitation coils (EM$_i$, $i = 1\sim5$).

Except for the vertical placement of the EM$_1$ with $[0,0,1]^T$ axial vectors $\mathbf{M}_{E1}$, the rest of the EMs are slightly tilted with axial vectors ($\mathbf{M}_{Ei}$, $i = 2\sim5$) and point in different directions. The orientation of the tilted EMs can also be specified by the Euler angles α, β, and γ. The PFG is symmetric with respect to the global coordinate axes. The origin of the Cartesian *XYZ* global coordinates is at the centroid of the combination of the four inclined EMs. Each excitation coil has a set of position and orientation vectors of $\mathbf{T}_{Ei}$ and $\mathbf{M}_{Ei}$(i =1, 2, 3, 4, 5), respectively.

Another agent in Fig. 1(a) is the sensing coil with a translation vector $\mathbf{T}_S$ and a pose vector $\mathbf{M}_S$. The relationship between the excitation coils and the induced EMF in the sensing coil is best understood with the transformation shown in Fig. 1(b). Illustrated by using EM$_1$ with its Cartesian coordinate (X_1, Y_1, Z_1) where the Z_1-axis passes through the axis of the EM$_1$ and the origin is at its centroid. The sensing

C.-Y. Lin et al.: Analytical and Experimental Investigation of EM Tracking System for Location and Orientation Estimation

IEEE *Access*

FIGURE 1. Schematics of the EM tracking system. (a) Pyramid field generator and sensing coil. (b) Sensing coil in excitation coil 1 coordinate. (c) Variables/parameters used in the modeling.

coil with six-DoF is described by the translation vector $\mathbf{t}_{s1}$ and axis vector $\mathbf{m}_{s1}$ related to the EM_1 coordinate system. A local Cartesian coordinate (X_s, Y_s, Z_s) is assigned to the sensing coil, where the axis vector is denoted as $\mathbf{m}_{s1}$. When EM_1 is activated, a harmonic current density J_e flows through the excitation coil, creating a harmonic magnetic field.

The varying $\mathbf{B}$ in space induces EMF in the sensing coil to be captured and analyzed. Detailed schematics for determining the EMF of the sensing coil from a single EM can be found in Fig. 1(c). The coordinate system of the EM transferred from Cartesian to cylindrical coordinate (R_1, θ_1, Z_1) is applied for modeling magnetic fields in the air generated from the cylindrical electromagnets. The $(a_{ei}, a_{eo}; a_e)$ are the inner radius, outer radius, and half-length of the excitation coil. The proposed DMF method divides the sensing coil with muti-turn into multiple layers of distributed elements. The MF passing through the coil is calculated by summarizing the $\mathbf{B}$ multiplied by the surface area. Therefore, the number of sensing coil winding turns along X_s and Z_s-axes are N_{sx} and N_{sz} individually. In Fig. 1(c), the coordinate of the sensing coil turns in X_s direction from the inner (a_{si}) to the outer radius (a_{so}) and in Z_s direction from the top (a_s) to the bottom (a_s) is described as $(X_{sj,k}, Y_{sj,k}, Z_{sj,k}, j = 1,2,\ldots N_{sx}, k = 1, 2, \ldots N_{sz})$. r_s, z_s are the positions in the radial and axial direction of the sensing coil. r_1, z_1 are the positions in the radial and axial direction of the first excitation coil. R_s, Z_s, R_1, Z_1 are normalized parameters. Characteristic geometrical parameters normalized to a_{eo} in x, y directions and a_e in z-direction in the dimensionless form are listed in Table 1.

The k value of the sensing coil's coordinate means the layer order of the sensing coil turns, and j represents the radius order of the cross-section circle, which encloses the axial vector of the coil $\mathbf{m}_s$. The MF is the inner product of the cross-section plane vector and the magnetic field for Faraday's law, so the scalar multiplication is operated by the z-component $\mathbf{B}$ and the elliptical area projecting the circular area to the XY-plane. The distributed element of the sensing coil is to divide a cross-section ellipse into tiny rectangles with infinitely short side dX_s, dY_s, and the area vector $\mathbf{S}_{j,k}$ can be determined to be $[0,0,1]^T$. Besides, the vectors $\mathbf{r}'$ and $\mathbf{r}$ extend from the origin to one line segment in the EM and one element of the sensing coil.

TABLE 1. Characteristic geometrical parameters.

Coordinate	Coil	Cross area
$(R, Z) = (r/a_{eo}, z/a_{eo})$	$\rho_i = a_{ei}/a_{eo}$	$dX_s = dx_s/a_{eo}$
$(X, Y, Z) = (x/a_{eo},\ y/a_{eo}, z/a_{eo})$	$\rho_a = a_e/a_{eo}$	$dY_s = dy_s/a_{eo}$
$(X_i, Y_i, Z_i) = (x_i/\ a_{eo}, y_i/a_{eo}, z_i/a_e)$	$\rho_{so} = a_{so}/a_{eo}$	$S_{j,k} = s_{i,k}/(a_{eo})^2$
$(R_s, Z_s) = (r_s/a_{eo}, z_s/a_e)$	$\rho_{si} = a_{si}/a_{eo}$	
$(X_s, Y_s, Z_s) = (x_s/\ a_{eo}, y_s/a_{eo}, z_s/a_e)$	$\rho_{sa} = a_s/a_e$	

A. MODELING OF ELECTROMOTIVE FORCE

The working principle of the EM tracking system is that the harmonic currents passing through the excitation coil generate the harmonic $\mathbf{B}$, and change the MF passing through the cross-sections of the sensing coil. The change of the MF leads to the EMF.

1) GOVERNING EQUATIONS

The excitation coil generates the $\mathbf{B}_E$ in the space with the $\mathbf{r}$ distance by the integral volume of the excitation coil is determined by Bio-Savart's law:

$$\mathbf{B}_E(\mathbf{r}) = \frac{\mu_0}{4\pi} \int_\Omega \frac{\mathbf{J}(\mathbf{r}') \times (\mathbf{r} - \mathbf{r}')}{|\mathbf{r} - \mathbf{r}'|^3} dV \qquad (1)$$

where $\mathbf{J}(\mathbf{r}')$ is the current density passing through the $\mathbf{r}'$ coordinate of the excitation coil with its volume Ω. The MF of the sensing coil is calculated by integrating the $\mathbf{B}$ over a cross-section area vector $\mathbf{S}$:

$$\Phi = \iint\limits_s \mathbf{B}_E(\mathbf{r}) \cdot d\mathbf{S} \qquad (2)$$

According to Faraday's law, the EMF V_b in the wire of the sensing coil is determined by the number of turns N_w times the time derivative of the MF:

$$V_b = -N_w \frac{d\Phi}{dt} \qquad (3)$$

For the cylindrical shape excitation coil, the $\mathbf{B}_E$ in (1) is expressed with the current density J_E with the cylinder coordinate:

$$\mathbf{B}_E = \eta_E(\mathbf{r}) J_E \qquad (4)$$

IEEE *Access*

C.-Y. Lin et al.: Analytical and Experimental Investigation of EM Tracking System for Location and Orientation Estimation

where $\eta_{\mathbf{E}}(\mathbf{r})$ depends on the winding geometry:

$$\eta_{\mathbf{E}}(\mathbf{r}) = \frac{\mu_o}{4\pi} \int_{\theta=0}^{2\pi} \int_{Z=-a_e}^{a_e} \int_{R=a_{ei}}^{a_{eo}} \frac{\mathbf{e}_\theta \times (\mathbf{r} - \mathbf{r}')}{|\mathbf{r} - \mathbf{r}'|^3} R \, dR \, dZ \, d\theta \quad (5)$$

The orientation $\mathbf{M}$ is determined by the rotation matrix $\mathbf{R} = \mathbf{R}_z(\gamma)\mathbf{R}_y(\beta)\mathbf{R}_x(\alpha)$ established by Euler angles α, β, γ from the Z-axis direction of the global coordinate $[0,0,1]^T$. The rotated axial vector $\mathbf{M}$ is rewritten as

$$\mathbf{M} = \begin{bmatrix} \cos\alpha \sin\beta \cos\gamma + \sin\alpha \sin\gamma \\ \cos\alpha \sin\beta \sin\gamma - \sin\alpha \cos\gamma \\ \cos\alpha \cos\beta \end{bmatrix} \quad (6)$$

As shown in Fig. 1(c), one cross-section ellipse of a sensing coil's layer is divided into tiny rectangles; the combined EMF in the sensing coil can be determined by summarizing all contributions from each circle and layer of the sensing coil turns. For the same layer or the same k value of the sensing coil turns coordinate $(X_{sj,k}, Y_{sj,k}, Z_{sj,k})$, the coordinate point encloses the axial vector of the coil $\mathbf{m}_s$ with the radius R_{sj} by a circle equation $X_s^2 + Y_s^2 = R_{sj}^2$. However, the translated and rotated sensing coil may change the cross-section equation of the coil to the ellipse equation, which the projection technique can solve. A circle with radius R_{sj} and centered at $(0, 0, Z_{sj,k})$, which the cylinder coordinate point $\mathbf{P}_s$ in the sensing coil coordinate can be expressed as $(R_{sj}\cos\theta, R_{sj}\sin\theta, Z_{sj,k})$. The position $\mathbf{P}_s$ of the circle rotated by α, and then γ with respect to the X-axis and Z-axis can be expressed as the position in the ellipse coordinate $\mathbf{P}_e$ via homogeneous transformation. Equations (7a) and (7b), as shown at the bottom of the page.

$\mathbf{R}_{se}$ is the rotation matrix transferred from the sensing coil coordinate to the ellipse coordinate. $\mathbf{R}_\gamma$, $\mathbf{R}_\alpha$ are the rotation around z and x-axis. Because the coordinate of the rotated $\mathbf{P}_e$ is relative to the coordinate system of the EM_1, the cross-sectional area of the sensing coil needs to project in the X_1-Y_1 plane for measuring magnetic flux. The following procedure obtains the ellipse form of the projected coordinate. The first step is to determine the ellipse central (x_0, y_0)

by the rotation matrix $\mathbf{R}_{se}$

$$\begin{bmatrix} x_0 \\ y_0 \\ 0 \end{bmatrix} = \mathbf{R}_{se} \begin{bmatrix} 0 \\ 0 \\ Z_{sj,k} \end{bmatrix} = \begin{bmatrix} Z_{sj,k} \sin\alpha \sin\gamma \\ -Z_{sj,k} \sin\alpha \cos\gamma \\ 0 \end{bmatrix}. \quad (8a)$$

The second step is to eliminate $Z_{sj,k}$ terms in x and y components of $\mathbf{P}_e$, rewritten as

$$\begin{cases} x - Z_{sj,k} \sin\alpha \sin\gamma \\ \quad = R_{sj} \cos\theta \cos\gamma - R_{sj} \sin\theta \cos\alpha \sin\gamma \\ y - (-Z_{sj,k} \sin\alpha \cos\gamma) \\ \quad = R_{sj} \cos\theta \sin\gamma + R_{sj} \sin\theta \cos\alpha \cos\gamma \end{cases} \quad (8b)$$

(8b) is multiplied by $cos(\gamma)$ and $sin(\gamma)$ in x and y terms individually then summing two equations as

$$x \sin\gamma - y \cos\gamma = -R_{sj} \sin\theta \cos\alpha + Z_{sj,k} \sin\alpha \quad (8c)$$

(8b) is multiplied by $sin(\gamma)$ and $cos(\gamma)$ in x and y terms individually then subtracting two equations as

$$x \cos\gamma + y \sin\gamma = R_{sj} \cos\theta. \quad (8d)$$

(8c) and (8d) are rewritten as the forms by adding ellipse central (x_0, y_0) to eliminate $Z_{sj,k}$

$$\begin{cases} (x - x_0) \sin\gamma - (y - y_0) \cos\gamma = -R_{sj} \sin\theta \cos\alpha \\ (x - x_0) \cos\gamma + (y - y_0) \sin\gamma = R_{sj} \cos\theta \end{cases} \quad (8e)$$

The square of the (8e) in left and right terms and summing is to obtain the ellipse equation with the center of the ellipse (x_0, y_0) can be represented as

$$[(x - x_0) \cos\gamma - (y - y_0) \sin\gamma]^2 + \frac{[(x - x_0) \sin\gamma - (y - y_0) \cos\gamma]^2}{\cos^2\alpha} = R_{sj}^2, \quad (8f)$$

where $x_o = Z_{sj,k} \sin\alpha \sin\gamma$, $y_o = -Z_{sj,k} \sin\alpha \cos\gamma$.

The MF for one ellipse can be calculated by taking the surface integral of the $\mathbf{B}$ over the enclosed ellipse with the sides dX_s and dY_s. The MF of the sensing coil Φ_E is derived

$$\mathbf{P}_e = \mathbf{R}_{se}\mathbf{P}_s,$$
$$\text{where } \mathbf{P}_s = \begin{bmatrix} R_{sj}\cos\theta & R_{sj}\sin\theta & Z_{sj,k} \end{bmatrix}^T$$
$$\mathbf{P}_e = \begin{bmatrix} x & y & z \end{bmatrix}^T$$
$$= \begin{bmatrix} R_{sj} \cos\theta \cos\gamma - R_{sj} \sin\theta \cos\alpha \sin\gamma + Z_{sj,k} \sin\alpha \sin\gamma \\ R_{sj} \cos\theta \sin\gamma + R_{sj} \sin\theta \cos\alpha \cos\gamma - Z_{sj,k} \sin\alpha \cos\gamma \\ R_{sj} \sin\theta \sin\alpha + Z_{sj,k} \cos\alpha \end{bmatrix} \quad (7a)$$

$$\mathbf{R}_{se} = \mathbf{R}_\gamma \mathbf{R}_\alpha$$
$$\text{where } \mathbf{R}_\gamma = \begin{bmatrix} \cos\gamma & -\sin\gamma & 0 \\ \sin\gamma & \cos\gamma & 0 \\ 0 & 0 & 1 \end{bmatrix}, \mathbf{R}_\alpha = \begin{bmatrix} 1 & 0 & 0 \\ 0 & \cos\alpha & -\sin\alpha \\ 0 & \sin\alpha & \cos\alpha \end{bmatrix}.$$

$$(7b)$$

C.-Y. Lin et al.: Analytical and Experimental Investigation of EM Tracking System for Location and Orientation Estimation

IEEE Access

by summing the MFs from layers of coils and integrating elements consisting of multiple ellipses with different radii.

$$\Phi_E = \sum_{k=1}^{Nsz} \Phi_{Ek} \tag{9}$$

Φ_{Ek} is the MF of the kth layer. N_{sz} is the number of layers.

$$\Phi_{Ek} = J_E \sum_{j=1}^{Nsx} \iint_S \eta_{\mathbf{E}}(\mathbf{r}) dY_s dX_s \tag{10}$$

With a sinusoidal current, the MF $\Phi_E = |\Phi_E| e^{-j\omega t}$, and using (3), the EMF is written as

$$V_E = -j\omega\Phi_E. \tag{11}$$

The harmonic response of EMF is shown to have a constant 90° phase shift from the input currents of the excitation coil. The MF passing through the sensing coil is done by first calculating a triple integral and then calculating a surface integral with area vector $\mathbf{S}$. (5) and (7b) are rewritten as

$$\Phi_{Ek}$$
$$= \frac{\mu_0 J_E}{4\pi} \sum_{j=1}^{Nsx} \iiint\int\int f(R, \theta, Z, X_s, Y_s) dR\, dZ\, d\theta\, dY_s dX_s \tag{12a}$$

where f
$$= R\frac{\mathbf{e}_\theta \times (\mathbf{r} - \mathbf{r}')}{|\mathbf{r} - \mathbf{r}'|^3}\mathbf{S}. \tag{12b}$$

The MF through the cross-section of the sensing coil is expressed in (2) and the integral form in (12a). The computation of definite multidimensional integration is time-consuming. Monte Carlo integration is a numerical method to evaluate approximate integral value at arbitrary points in Ω. As the number of sampling points increases, the value will converge to an exact number. $\Omega \in \mathbb{R}^5$ in (12a) is composed of the five integral variables to form its volume V_j. The integral volume equals the multiplication of the cylinder volume of the excitation coil and the jth cross-sectional ellipse of the sensing coil. The sample points $\mathbf{X}_i$ are randomly selected with equal probability in the domain Ω with the total number N. The integrand $f(R,\theta,Z,X_s,Y_s)$ is turned into a discrete function $f(\mathbf{X}_i)$. The mean is adopted by summing discrete values and dividing by N. Φ_{Ek} can be approximated by

$$\Phi_{Ek} = \frac{\mu_0 J_E}{4\pi} \sum_{j=1}^{Nsx} \frac{V_j}{N} \sum_{i=1}^{N} f(\mathbf{X}_i). \tag{13}$$

The Monte Carlo integration method, sampling random points within the integration region to take the mean value, is used to speed up the computational time.

B. ELECTROMAGNETIC TRACKING SYSTEM DESIGN
The hardware of the proposed EM tracking system is illustrated in Fig. 2. The data acquisition (DAQ) system is utilized as the interface that sends the signals to the current amplifier
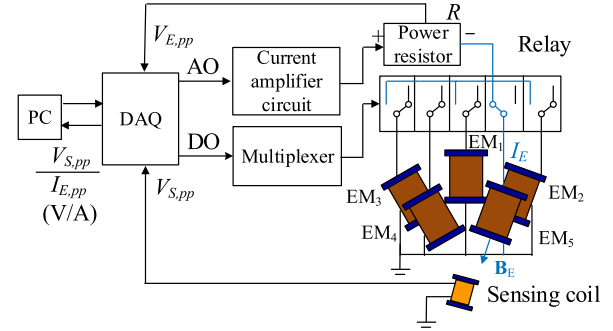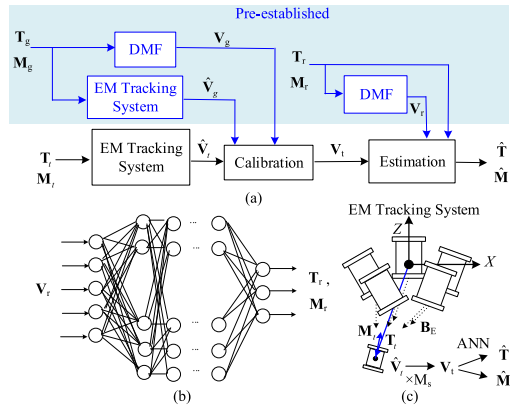

FIGURE 2. Illustration of the EM tracking system.

by the analog output (AO) and the multiplexer connected to the relay by the digital output (DO) to select electromagnets (EMs) in turns from EM_1 to EM_5. The current (I_E) flowing through the EMs can be measured by the cross peak-to-peak voltage (V_E) value of the R ohm power resistor with Ohm's law. The EMs with current (I_E) generate the $\mathbf{B}_E$ in space and further the EMF (V_S) in the sensing coil. The peak-to-peak current $I_{E,pp}$ and voltage $V_{S,pp}$ of the sinusoidal signals can be read through the analog input (AI) to perform division to normalize the current input (I_E) to one ampere.

In Fig. 3(a), the algorithm can be separated into two parts: the precomputed reference map shown in the blue shaded region and the actual procedures marked in black. The ultimate goal of the system is to calculate the pose and position vector of the sensing coil based on the induced EMFs. Whether the data comes from the forward DMF model or the experiments, there are two ways to relate the EMFs to the corresponding location and orientation. The theoretical values from the forward model with ideal assumptions can be produced more efficiently than the experimental data. It is also immune to outside noises that could distort the results. Considering the requirements for a large amount of data to train the neural network for the inverse calculation, the theoretical values are more advantageous, as the experiments lack flexibility and are more time-consuming. However, a mapping relationship between these two sets of values must first be found to use the ANN model trained with theoretical values to perform estimations based on experimental data.

This relationship is first investigated by comparing the values from the DMF model and the experiments from the same sensing coil configurations. The sensing coil is set to be in a set of locations $\mathbf{T}_g$ with a certain orientation $\mathbf{M}_g$ in both the DMF model and experiments. The EMF values from the former are denoted as Vg while the ones obtained empirically would be called $\hat{\mathbf{V}}_g$. With both $\mathbf{V}_g$ and $\hat{\mathbf{V}}_g$ and knowing the identical setup $\mathbf{T}_g$ and $\mathbf{M}_g$, a function can be found by performing least square fitting that could transform $\hat{\mathbf{V}}_g$ to $\mathbf{V}_g$, and this step is referred to as calibration.

Aside from the calibration, which relates the experimental EMF values to the theoretical ones, an estimation process is needed to calculate the pose and position vectors based on the EMF values. This is done by employing an ANN

IEEE *Access*

C.-Y. Lin et al.: Analytical and Experimental Investigation of EM Tracking System for Location and Orientation Estimation

FIGURE 3. Algorithm of the location and orientation estimation(a) Flowchart. (b) ANN structure for the estimation process. (c) Actual test process.

structure trained only with the data from the DMF forward model. Using the DMF model, relative random and massive sets of location and orientation vectors, denoted as $\mathbf{T}_r$ and $\mathbf{M}_r$, are simulated, and the corresponding EMF $\mathbf{V}_r$ are obtained. These values are then used as the training data for the ANN model with the EMFs as the input and the spatial information of the receiving coil as the output shown in Fig. 3(b). For the convenience of variable description in Fig. 3, (14a)-(14d) is to express the matrix data set $\hat{\mathbf{V}}_g$, $\mathbf{T}_k$, $\mathbf{M}_k$, $\mathbf{V}_k$ ($k \in$ g, r). n_g is the grid number from the DMF model and the experiments from the same configuration. n_r is the number of random data sets constructed by the DMF model.

The calibration and estimation process are conducted in series in actual testing. First, a sensing coil with an unknown position $\mathbf{T}_t = [T_{tx}, T_{ty}, T_{tz}]^T$ and pose $\mathbf{M}_t = [M_{tx}, M_{ty}, M_{tz}]^T$ would measure five EMF $\hat{\mathbf{V}}_t = \begin{bmatrix} \hat{v}_{t1} & \hat{v}_{t2} & \hat{v}_{t3} & \hat{v}_{t4} & \hat{v}_{t5} \end{bmatrix}^T$, induced from the $\mathbf{B}_E$ in the air from the excited PFG, in the tracking system illustrated in Fig. 3(c). This value is then mapped to the corresponding theoretical $\mathbf{V}_t = [V_{t1}, V_{t2}, V_{t3}, V_{t4}, V_{t5}]^T$ by multiplying the gains $\mathbf{M}_s$ in the calibration process. Finally, transformed Vt then goes through two ANN models to perform the inverse calculation, which yields the estimation results $\hat{\mathbf{T}} = \begin{bmatrix} \hat{t}_x & \hat{t}_y & \hat{t}_z \end{bmatrix}^T$ and $\hat{\mathbf{M}} = \begin{bmatrix} \hat{m}_x & \hat{m}_y & \hat{m}_z \end{bmatrix}^T$

$$\hat{\mathbf{V}}_g \in R\left(5 \times n_g\right) = \begin{bmatrix} \hat{v}_{g1,1} & \hat{v}_{g1,i} & \hat{v}_{g1,n_g} \\ \hat{v}_{g2,1} & \hat{v}_{g2,i} & \hat{v}_{g2,n_g} \\ \hat{v}_{g3,1} & \cdots & \hat{v}_{g3,i} & \cdots & \hat{v}_{g3,n_g} \\ \hat{v}_{g4,1} & \hat{v}_{g4,i} & \hat{v}_{g4,n_g} \\ \hat{v}_{g5,1} & \hat{v}_{g5,i} & \hat{v}_{g5,n_g} \end{bmatrix} \tag{14a}$$

$$\mathbf{T}_k \in R\left(3 \times n_k\right) = \begin{bmatrix} t_{kx,1} & t_{kx,i} & t_{kx,n_k} \\ t_{ky,1} & \cdots & t_{kx,i} & \cdots & t_{ky,n_k} \\ t_{kz,1} & t_{kx,i} & t_{kz,n_k} \end{bmatrix} \tag{14b}$$

$$\mathbf{M}_k \in R\left(3 \times n_k\right) = \begin{bmatrix} m_{kx,1} & m_{kx,i} & m_{kx,n_k} \\ m_{ky,1} & \cdots & m_{kx,i} & \cdots & m_{ky,n_k} \\ m_{kz,1} & m_{kx,i} & m_{kz,n_k} \end{bmatrix} \tag{14c}$$

$$\mathbf{V}_k \in R\left(5 \times n_k\right) = \begin{bmatrix} v_{k1,1} & v_{k1,i} & v_{k1,n_k} \\ v_{k2,1} & v_{k2,i} & v_{k2,n_k} \\ v_{k3,1} & \cdots & v_{k3,i} & \cdots & v_{k3,n_k} \\ v_{k4,1} & v_{k4,i} & v_{k4,n_k} \\ v_{k5,1} & v_{k5,i} & v_{k5,n_k} \end{bmatrix} \tag{14d}$$

III. NUMERICAL VERIFICATION AND VALIDATION

The design method for the EM tracking system is best illustrated numerically by software. Numerical investigations for both the DMF method and inverse DMF models are performed:

1) Numerical verification for the DMF method outlining induced $\mathbf{B}$, MF, and EMF in the sensing coil. Both the vertical and tilted EM with various combinations for locations and poses estimation of the sensing coil are involved in investigating the effects of different spatial configurations.

2) Numerical validation of the ANN-based estimation for the location and orientation of the sensing coil through the DMF method simulated EMFs by the PFG.
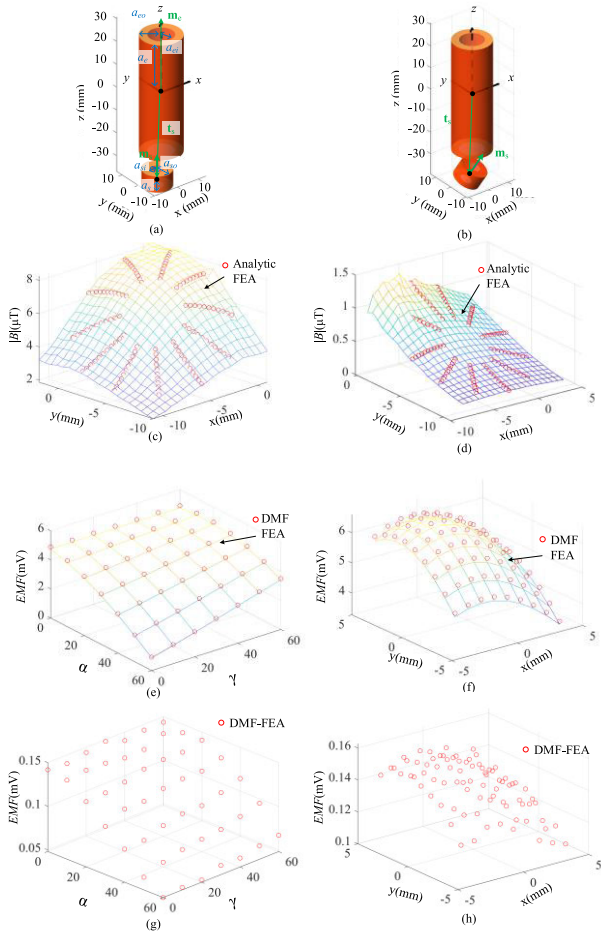
A. NUMERICAL VERIFICATION OF B IN AIR, EMF OF A SENSING COIL

With the help of the magnetic and electric field interface of COMSOL Multiphysics 5.0, the DMF method is compared with the FEA results. A vertical excitation coil and a tilted coil of the PFG are utilized to numerically verify the effects of translation and angular displacement.

1) A PAIR OF EXCITATION AND SENSING COIL

With the support of Commercial FEA software COMSOL, as shown in Fig. 4, the validity of the DMF method is compared with the FEA results for a pair of excitation and sensing coils in the preliminary verification. Thus, further development of the EM tracking system can be conducted. The simulation configurations in three-dimensional space are shown in Fig. 4(a), (b). The vertical excitation coil above is fixed to the origin and is excited with 1A, 20kHz external current input. The tilted sensing coil is free to move in the xy-plane and rotate around any axis. The simulation parameters are listed in Table 2. Fig. 4(a), (c), (e), and (g) discuss the effects of rotation for a vertical sensing coil, and Fig. 4(b), (d), (f), and (h) discuss the effects of translation for a tilted sensing coil. The z-directional magnitudes of the $\mathbf{B}$ ($|\mathbf{B}|$) are induced on the upper surface of the sensing coil for Fig. 4(a), (b) shown in Fig. 4(c), (d), respectively.

For a sensing coil with forty-nine directions of rotation around x- and z axes (by α and γ degrees, respectively) located at $\mathbf{t}_s$ point on the xy-plane, the estimated EMFs are shown in Fig. 4(e). The measured EMFs of a sensing coil with a constant orientation $\mathbf{m}_s$ and xy-plane displacement of eighty-one places are shown in Fig. 4(f). Fig. 4(g), (h) show the deviation between the DMF method and FEA simulation for Fig. 4(e), (f). The Root Mean Square Error (RMSE) in (8c) determines the discrepancy, where N is the number of data. The RMSEs are 0.3556 for the 49 points on orientation

C.-Y. Lin et al.: Analytical and Experimental Investigation of EM Tracking System for Location and Orientation Estimation

IEEE Access

FIGURE 4. Numerical investigation of a pair of excitation and sensing coils. (a, b) Simulation configuration. (c, d) z-component B on the top surface of the sensing coil. (e) Effects of rotation for induced EMFs in the sensing coil. (f) Effects of translation for induced EMFs in the sensing coil. (g) The EMF error map for rotating sensing coil. (h) The EMF error map for translating sensing coil.

point estimations and 0.4351 for the 81 points on location estimations, respectively.

$$RMSE = \sqrt{\frac{1}{N}\sum_{i=1}^{N}\left(V_{\text{DMF},i} - V_{\text{FEA},i}\right)^2} \qquad (15)$$

In the simulation, N is chosen as 10^7 in (8a) for the Monte Carlo integration, and the number of turns for the sensing coil is 220. In (7b)-(7b), the cross-sectional area of the coil and the number of turns of the coil are positively correlated with the strength of the induced EMF, which dictates the operation range. However, the size of the sensing coil also grows as the turns increase. Considering the future surgical application, the sensing coil used in the DMF validation is designed to have 220 turns. The number of turns of the excitation coil is designed to be 2325, which is enough to have a magnetic field of about 10μT still when the distance from the center of the coil is 30mm in Fig. 4(c). Then, to place compact multi-directional magnetic field transmitters, the

slender excitation coil conforms to the design for the inner diameter, outer diameter, and height of the excitation coil. The simulation is computed on a PC Intel Core i7-10700F, GPU GTX 1650 with 4G RAM. The computational time is 7 seconds for calculating one EMF value.

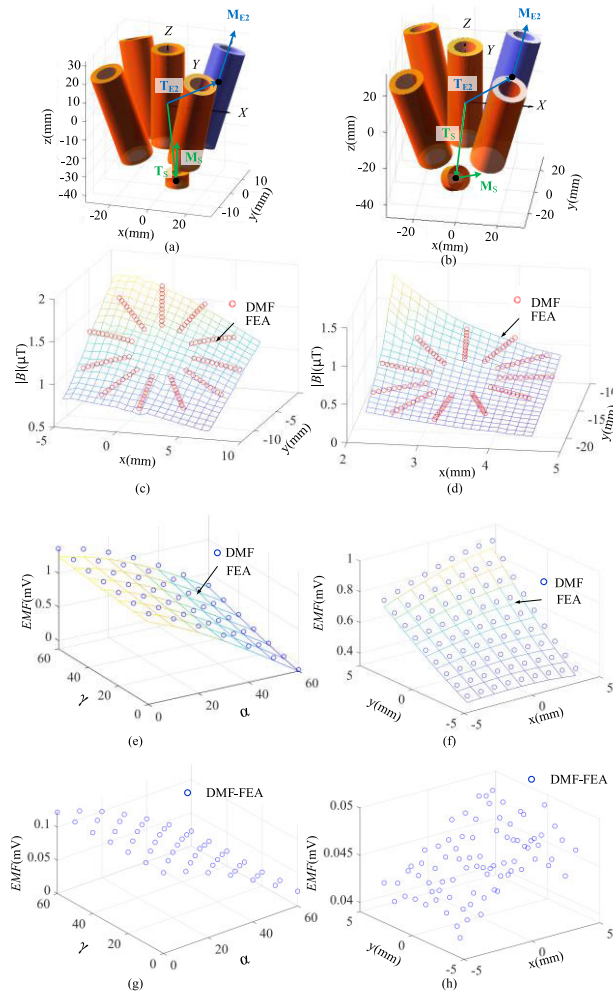**TABLE 2.** Parametric values of EM and sensing coil.

Excitation coil			
Geometry (mm)	Current	Location, Orientation	
a_{eo}=8.5, a_{ei}=5.25, a_e=25, N_E=2325	I_0 (A) =1 f(kHz) = 20	$\mathbf{t}_e$=[0,0,0]$^\text{T}$ $\mathbf{m}_e$=[0,0,1]$^\text{T}$	
Sensing coil			
Geometry(mm)	a_{so}=6.031, a_{si}=2.5, a_s=7, N_{sx}=11, N_{sz}=20		
	Location	Orientation	
	$\mathbf{t}_s$=[t_{sx}, t_{sy}, t_{sz}]$^\text{T}$	Φ_s=(α_s, β_s, γ_s)	$\mathbf{m}_s$= [m_{sx},m_{sy},m_{sz}]$^\text{T}$
Fig. 4(a), (c)	[−4, −4, −33.3]$^\text{T}$	(30°, 0°, 40°)	[0.32, −0.38, 0.87]$^\text{T}$
Fig. 4(e)	−4≤ t_{sx} ≤4, −4≤ t_{sy} ≤4, t_{sz}=−33.3		
Fig. 4(b), (d)	[−5, −4, −33.3]$^\text{T}$	(0°, 0°, 0°)	[0, 0, 1]$^\text{T}$
Fig. 4(f)		0°≤α≤60°, β=0°, 0°≤γ≤60°	

2) PYRAMID FIELD GENERATOR AND A SENSING COIL

Closer to practical use, Fig. 5 illustrates the simulation for the excitation of one coil from the PFG. Fig. 5(a), (c), and (e) illustrate the effects of rotation for a vertical sensing coil, and Fig. 5(b), (d), and (f) discuss the effects of translation for a tilted sensing coil. In the simulation, EM$_2$ is excited, as shown in Fig. 5(a), (b). The position $\mathbf{T}_E$ and orientation $\mathbf{M}_E$, a unit vector that could be calculated from Φ_E via (6), are listed in Table 3. All the coils, including the excitation and the sensing coils, have the same geometry, and the dimension can be found in Table 2. Similar to the location and orientation simulation of a pair of excitation and sensing coils, in which $\mathbf{t}_s$ equals $\mathbf{T}_S$ and $\mathbf{m}_s$ equals $\mathbf{M}_S$, the sensing coil is free to rotate in Fig. 5(a) and free to translate in Fig. 5(b). The simulated |B|, with the z-component generated on the upper surface of the sensing coil, and the induced EMF in the sensing coil in the configuration are shown in Fig. 5(c), (d), and Fig. 5(e), (f), respectively. The EMF error maps, displayed in Fig. 5(g), (h), between the DMF method and FEA simulation for rotating and translating sensing coil are utilized to indicate the result deviation. The RMS errors of the calculated EMFs are shown in Fig. 5(g) and (h) are 0.2649 and 0.1403 by the number of 49 and 81 data points. The verification of the DMF method, which applies Monte Carlo integration, shows the accordance result of the **B** and EMF between the DMF method and FEA simulation in the effects of translated and angular displacement.

B. NUMERICAL VALIDATION OF ANN FOR LOCATION AND POSE ESTIMATION

The five excitation coils in a pyramid arrangement form a field generator, as displayed in Fig. 6(a), and the geometries

IEEE Access

C.-Y. Lin et al.: Analytical and Experimental Investigation of EM Tracking System for Location and Orientation Estimation


FIGURE 5. Numerical investigation of the PFG. (a, b) Simulation configuration. (c, d) Z-component B on the top surface of the sensing coil. (e) Effects of rotation for induced EMFs in the sensing coil. (f) Effects of translation for induced EMFs in the sensing coil. (g) The EMF error map for rotating sensing coil. (h) The EMF error map for translating sensing coil.

TABLE 3. Position and orientation of EMs of PFG.

EM_i	$\mathbf{T}_E$ (mm)	Φ_E(degree)	$\mathbf{M}_E$
1	$[0, 0, 5]^T$	$(0, 0, 0)$	$[0, 0, 1]^T$
2	$[18.5, 18.5, 0]^T$	$(-20, 0, -45)$	$[0.242, 0.242, 0.940]^T$
3	$[-18.5, 18.5, 0]^T$	$(-20, 0, 45)$	$[-0.242, 0.242, 0.940]^T$
4	$[-18.5, -18.5, 0]^T$	$(20, 0, -45)$	$[-0.242, 0.242, -0.940]^T$
5	$[18.5, -18.5, 0]^T$	$(20, 0, 45)$	$[0.242, -0.242, 0.940]^T$

of the excitation coil and sensing coil have the same values as listed in Table 2, and 3. Fig. 6(b) shows the estimated four position and orientation results by using the structure of the ANN for estimation in Fig. 3(b). The five excitation coils in the filed generator are fired one by one with sinusoidal input at a 20KHz certain frequency to produce a change in the **B** for inducing the EMF to be measured.

The architecture benefits from abundant input data. The estimation of $\mathbf{T}_S$ and $\mathbf{M}_S$ are separated into two ANN for more accurate results, as shown in Fig. 3(b). Both models
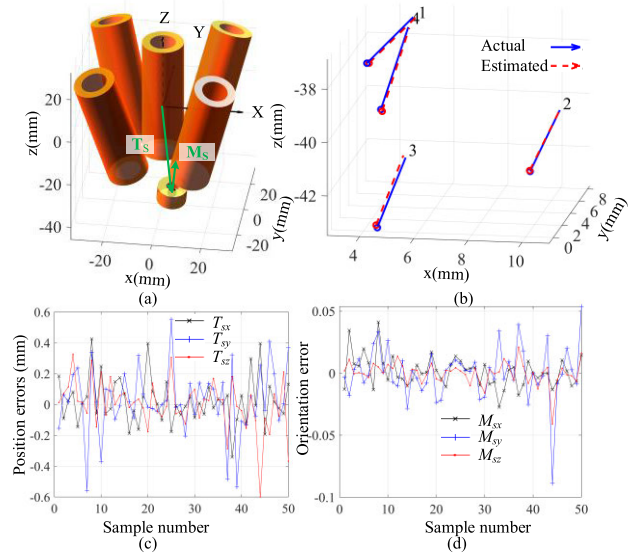
FIGURE 6. Simulation for inverse estimation. (a) Simulation setup. (b) Estimation results. (c) Position errors of fifty samples. (d) Orientation errors of fifty samples.

TABLE 4. Simulation results.

i		Actual T(mm)	Actual M	Estimated T(mm)	Estimated M	Error T(mm)	Error M
1	x	2.81	0.56	2.88	0.57	0.07	0.01
	y	8.28	−0.54	8.33	−0.53	0.05	0.01
	z	−39.13	0.62	−39.13	0.63	0	0.01
2	x	9.59	0.39	9.59	0.39	0	0
	y	3.51	−0.51	3.42	−0.50	−0.09	0.01
	z	−41.85	0.77	−41.80	0.77	0.05	0
3	x	4.41	0.36	4.37	0.35	−0.04	−0.01
	y	0.60	0.42	0.58	0.43	−0.02	0.01
	z	−43.48	0.84	−43.39	0.83	0.09	−0.01
4	x	3.30	0.32	3.36	0.31	0.06	−0.03
	y	8.46	−0.22	8.37	−0.21	−0.09	0.01
	z	−40.89	0.92	−40.93	0.93	−0.04	0.01
Error RMSE: $\mathbf{T}=[0.04, 0.06, 0.05]^T$ (mm), $\mathbf{M}=[0.01, 0.01, 0.01]^T$							

take input from the same set of the DMF method. The two ANNs have three hidden layers with 50 neurons for each layer. The input data is generated in two stages. The first stage is to generate uniform data of EMF within a pre-set range: $T_{Sx}(0\sim15mm)$, $T_{Sy}(0\sim15mm)$, $T_{Sz}(-49\sim39mm)$, $\alpha_S(0\sim60°)$, $\gamma_S(0\sim60°)$. The intervals of T_{Sx}, T_{Sy} are 3 mm, and 2 mm for T_{Sz}. The intervals of α_S, γ_S are 15°. The shape of the induction coil is cylindrical and axisymmetric. Thus, the rotation angle β is not considered and is set to 0°. The number of uniform data is 5400. The second stage is to increase the number of data sets up to 7500 random data within the preset range. Out of a total of 112900 sets of data, 70% of which is used for training, 15% for validation, and the remaining 15% for testing. Fig. 6(c) and (d) show the location and orientation error for the fifty samples. The position errors are less than 0.6 mm and the orientation errors fall below 0.05. Table 4 indicates the four of the fifty samples' position and

C.-Y. Lin et al.: Analytical and Experimental Investigation of EM Tracking System for Location and Orientation Estimation

IEEE *Access*

orientation estimation results of the sensing coil shown in Fig. 6(b). The error of the position is less than 0.1 mm, and the orientation is less than 0.05. The RMSEs of the errors for $\mathbf{T}_S$ and $\mathbf{M}_S$ are $[4 \times 10^{-2}, 6 \times 10^{-2}, 5 \times 10^{-2}]^T$(mm) and [0.01, 0.01, 0.01]^T, respectively. The small RMSEs demonstrate the potential of the ANN-based estimation. The effectiveness of this estimation method using simulated data paves the way for similar techniques to be used in the practical world with measured EMFs from the sensing coil to obtain the six-DOF parameters.

IV. EXPERIMENTAL RESULTS AND DISCUSSION

The design of the proposed EM tracking system has been experimentally investigated. Fig. 7 shows the experimental setup of the EM tracking system. In Fig. 7(a), the PFG consisted of five excitation coils with the same geometry parameters as the simulation configuration listed in Table 2 and 3, and the 3D printed PLA was used to form fixed positions and orientations to combine five coils as shown in Fig. 7(c). The optical table was used as the base for installing the PFG on the elevated acrylic bracket. The sinusoidal signal was generated analog output by the NI-9262 of the DAQ system to the current amplifier. The analog inputs of the peak-to-peak values of cross voltages through EMs and EMFs from the sensing coil are simultaneously received by the NI-9223 to perform division to normalize the current input to one ampere. Besides, the USB-6216 was used as digital voltage output to control the multiplexer (CD4051) and relay circuit for the current switching of the EMs. The relay was switched by a multiplexer so that the amplified current excited the five EMs of the PFG in turn.

In Fig. 7(b), the manual precision stage was capable of translational and rotational movements in all three directions (X, Y, Z) and one Euler angle (γ). In addition, the angle (α) was rotated by the servo motor, controlled by Arduino Nano, shown in Fig. 7(c). The motor would be turned off after turning to the target angle to reduce the influence of the magnetic field. Fig. 7(d) shows the electronic hardware corresponding to the structure of the EM tracking system shown in Fig. 2. The power resistor was connected after the current amplifier to measure the EMF by Ohm's Law through the current flowing in the excitation coil. The relays and multiplexers control the amplified current output to feed to a certain excitation coil. The current waveform is sensed via a power resistor in series with the coil. Arduino Nano is utilized to control the rotation angle of the sensing coil α, as shown in Fig. 7(c).

Due to the manufacturing error in the coil winding, the actual value of the current density J_E can not be calculated from the geometry of the coil, so the calculation of the induced EMF of the sensing coil had errors between the DMF method and the EM tracking system. The cross-sectional area of an ideal coil is assumed to be arranged orderly, and wire diameter is used to calculate. However, the coils in real life are often wound in a less orderly manner. Some gaps exist between the wires in the cross-section of the coil. Therefore,
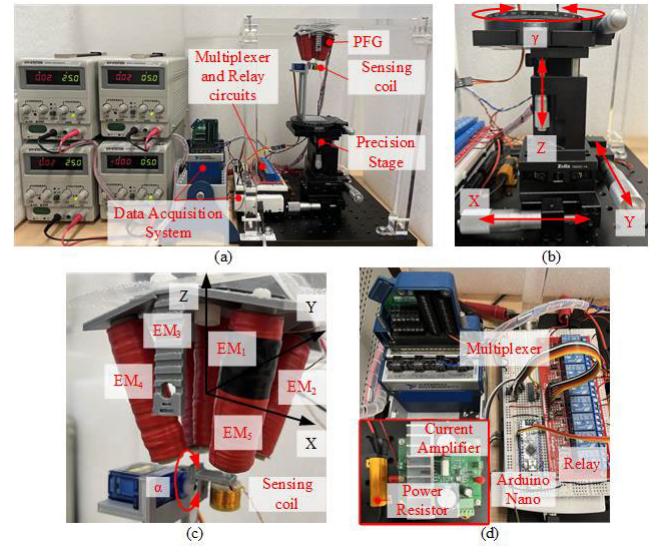
FIGURE 7. EM tracking system. (a) Experimental setup. (b) XYZ linear and rotational stages. (c) Close-up of PFG, the sensing coil, and the servo motor. (d) Related circuits.

the actual density of excitation coils is difficult to estimate, so the discrepancy between an ideal and an actual coil tends to accumulate as the number of coils increases. The calibration process aims to reconcile the difference between the experimental $\hat{\mathbf{V}}_t$ and the theoretical EMFs $\mathbf{V}_t$ by a gain values $M_{sj}, (j = 1,2,3,4,5)$ gain of the experimental EMFs ($\hat{\mathbf{V}}_t$) to transfer calibrated EMFs ($\mathbf{V}_t$) into the estimation process. The relation between the EM tracking system and ANN-based estimation models was constructed by the corresponding EMFs of the DMF method ($\mathbf{V}_g$) and the EM tracking system ($\hat{\mathbf{V}}_g$) when a total of n_g equaled 256 for different positions $\mathbf{T}_g$, from 0 to 6mm with 3mm increments in X and Y directions and from −39 to −43 mm with −2mm increments in the Z direction, and poses $\mathbf{M}_g$ which angles α_S and γ_S were (0º, 15º, 30º). The relationship between the magnitudes of the model and experimental data was described in (8d). $\hat{V}_{tj}$, V_{tj} denoted the magnitudes of the experimental and model data for j^{th} gains M_{Sj} ($j = 1, 2, 3, 4, 5$) for the five EMFs, which were obtained by the least squares method with $\hat{\mathbf{V}}_g$ and $\mathbf{V}_g$ in (17a), (17b).

$$V_{tj} = M_{Sj}\hat{V}_{tj} \quad (16)$$

$$\frac{dE_j}{dM_{Sj}} = 0, \text{ where } \mathrm{E}_j = \sum_{i=1}^{ng}\left(V_{gji} - M_{Sj}\hat{V}_{gji}\right)^2 \quad (17a)$$

$$M_{Sj} = \frac{\sum_{i=1}^{ng} V_{gji}\hat{V}_{gji}}{\sum_{i=1}^{ng} \hat{V}_{gji}^2} \quad (17b)$$

Therefore, the gains of the five EMFs measured for the calibration process are 0.169, 0.168, 0.163, 0.205, 0.153. In the preliminary experiment, four test points were used as

verification, and the pose and position of the sensing coil were adjusted by the translation and rotation platform as shown in Table 4. The test points received the magnetic field of the PFG in sequence to obtain five induced electromotive forces $\hat{V}_{tj}$, and the corrected V_{tj} is obtained by the gains of the calibration process. Fig. 8(a) indicates the comparison of the calibrated EMFs V_t and the DMF method result as four testing positions T_t and orientations M_t, shown in Fig. 8(b). According to the pre-established ANN-based estimation constructed in Section II-B, calibrated EMFs V_t were fed into the estimation process of the position and orientation models, respectively. Table 5 shows the estimation results and errors with the calibration and estimation process. The errors of $\hat{T}$ are within 0.6 mm for each direction and $\hat{M}$ are less than 0.02, and use the inner product to calculate the angle error of the orientation of the experiment and the simulation. The error is maintained within 1.5 degrees. The RMSEs of errors for T_s and M_s are $[0.08, 0.10, 0.45]^T$ (mm) and $[0.04, 0.01, 0]^T$, respectively.
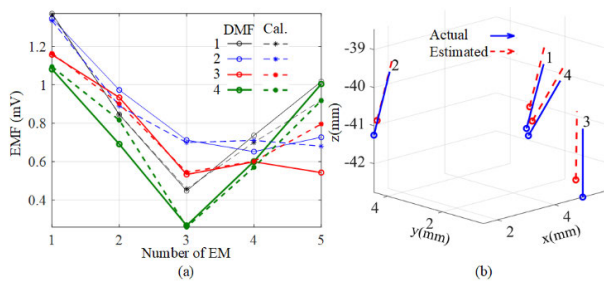

FIGURE 8. The experimental results of position and orientation estimation. (a) Calibrated EMFs. (b). Estimated results.

TABLE 5. Experimental results.

i		Testing T (mm)	M	Estimated T (mm)	M	Error T (mm)	M	$\theta(°)$
1	x	3.5	0.11	3.64	0.09	0.14	−0.02	
	y	1	−0.23	1.03	−0.23	0.03	0	1.138
	z	−40.75	0.97	−40.22	0.97	0.53	0	
2	x	1.5	0.07	1.56	0.07	0.06	0	
	y	4.5	−0.25	4.46	−0.25	−0.04	0	0
	z	−41.25	0.97	−40.86	0.97	0.39	0	
3	x	5	0	4.90	0.01	−0.10	0.01	
	y	0.5	0	0.65	−0.02	0.15	−0.02	1.281
	z	−42.75	1	−42.31	1.00	0.44	0	
4	x	5.5	0.17	5.47	0.19	−0.03	0.02	
	y	3	−0.47	2.84	−0.46	−0.16	0.01	1.276
	z	−41.75	0.87	−41.33	0.87	0.42	0	
Error RMSE: T=[0.08, 0.10, 0.45]^T (mm), M=[0.04, 0.01, 0]^T								

V. CONCLUSION

The prototype of the EM tracking system to target the location and orientation of the sensing coil using the procedure including the DMF method, system design, least square method, and ANN model has been presented. The numerical software COMSOL has verified the DMF modeling of electromagnetic force for the feasibility of the EM tracking system. The theoretical basis of this EM tracking system—a closed-form solution of the harmonic responses of the EMF induced in

the rotated sensing coils acquired using the DMF method was verified by comparing it with the computed solutions obtained using commercial FEA software. The RMSEs of electromagnetic force are within 0.5 on estimations. The computational time for computing the EMF of the sensing coil is about 7 seconds. The forward data of the DMF method enables to train ANN-based estimation model, presented to predict the position and orientation by feeding the simulated EMF using the random and massive sets of location and orientation vectors.

Experiments were conducted on the sensing coil within the range of $[T_{Sx}, T_{Sy}, T_{Sz}]^T = [0\sim6, 0\sim6, -39\sim -43]^T$ mm, and the angles of α_S and γ_S were from 0° to 30° with linear increments. The calibration process was established through the least squares method to connect the EMFs generated by the EM tracking system and the DMF method. In the experiment, the four test points have been preliminarily validated by calibration. The RMSEs for location and orientation are $[0.08, 0.10, 0.45]^T$ (mm) and $[0.04, 0.01, 0]^T$, respectively. The pose errors are within 1.5 degrees. The small RMSEs of errors validate the effects of the proposed EM tracking system on location and orientation estimation.

Our work presents the preliminary design and development process of a prototype of the EM tracking system. The tracking system can be enhanced in future work to increase the estimation limit speed, improve its accuracy, and augment the operation range. In terms of the estimation speed, both the hardware and the software of the system can be improved. Currently, the time multiplex system requires three seconds for a round of excitation, which could be accelerated by adopting a frequency multiplex system. In this case, all the EMs can be excited at once with different excitation frequencies, and the induced EMF as a result of the excitation from a specific coil can be isolated by the Fast Fourier Transform. However, the increased cost of the system is taken to be considered because of the need for multiple current amplifiers. The ANN models are tested as a precursor to more advanced models that could be included in future studies.

There are also several ways to enhance the accuracy of the system. More data can be generated with the DMF model for the training of the ANN structure. The calibration process can also be optimized. In this study, the gain factor is calculated offline with least square fitting based on the measurements of 256 sets of location and orientation vectors, which is only done once before all the subsequent testing. However, the gain could be different in the actual testing; therefore, a calibration process prior to each individual testing could be a boon to the accuracy. A calibration module can facilitate this procedure with carefully placed holes and cavities to position the sensing coil precisely. The gain factor can be calculated with the precomputed theoretical values.

REFERENCES

[1] A. M. Franz, T. Haidegger, W. Birkfellner, K. Cleary, T. M. Peters, and L. Maier-Hein, "Electromagnetic tracking in medicine—A review of technology, validation, and applications," *IEEE Trans. Med. Imag.*, vol. 33, no. 8, pp. 1702–1725, Aug. 2014.

C.-Y. Lin et al.: Analytical and Experimental Investigation of EM Tracking System for Location and Orientation Estimation

IEEE *Access*

[2] H.-X. Xu, M.-D. Lu, L.-N. Liu, and L.-H. Guo, "Magnetic navigation in ultrasound-guided interventional radiology procedures," *Clin. Radiol.*, vol. 67, no. 5, pp. 447–454, May 2012.

[3] S. Vaezy and V. Zderic, *Image-Guided Therapy Systems*. Washington, DC, USA: Artech House, 2009.

[4] D. J. Grand, M. A. Atalay, J. J. Cronan, W. W. Mayo-Smith, and D. E. Dupuy, "CT-guided percutaneous lung biopsy: Comparison of conventional CT fluoroscopy to CT fluoroscopy with electromagnetic navigation system in 60 consecutive patients," *Eur. J. Radiol.*, vol. 79, no. 2, pp. 133–136, Aug. 2011.

[5] J. Krücker, S. Xu, A. Viswanathan, E. Shen, N. Glossop, and B. Wood, "Clinical evaluation of electromagnetic tracking for biopsy and radiofrequency ablation guidance," *Int. J. Comput. Assist. Radiol. Surg.*, vol. 1, pp. 169–171, Jan. 2006.

[6] M. J. Wallace, S. Gupta, and M. E. Hicks, "Out-of-plane computed-tomography-guided biopsy using a magnetic-field-based navigation system," *CardioVascular Interventional Radiol.*, vol. 29, no. 1, pp. 108–113, Feb. 2006.

[7] K. A. Khan, P. Nardelli, A. Jaeger, C. O'Shea, P. Cantillon-Murphy, and M. P. Kennedy, "Navigational bronchoscopy for early lung cancer: A road to therapy," *Adv. Therapy*, vol. 33, no. 4, pp. 580–596, Apr. 2016.

[8] E. J. Hermann, H.-H. Capelle, C. A. Tschan, and J. K. Krauss, "Electromagnetic-guided neuronavigation for safe placement of intraventricular catheters in pediatric neurosurgery," *J. Neurosurgery, Pediatrics*, vol. 10, no. 4, pp. 327–333, Oct. 2012.

[9] F. Kral, E. J. Puschban, H. Reichelmann, F. Pedross, and W. Freysinger, "Optical and electromagnetic tracking for navigated surgery of the sinuses and frontal skull base," *Rhinology J.*, vol. 49, no. 3, pp. 364–368, Aug. 2011.

[10] T. Peters and K. Cleary, *Image-Guided Interventions: Technology and Applications*. Berlin, Germany: Springer-Verlag, 2008.

[11] P. Shenoy, V. Sompur, and V. Skm, "Methods for measurement and analysis of full hand angular kinematics using electromagnetic tracking sensors," *IEEE Access*, vol. 10, pp. 42673–42689, 2022.

[12] W. Kim, J. Song, and F. C. Park, "Closed-form position and orientation estimation for a three-axis electromagnetic tracking system," *IEEE Trans. Ind. Electron.*, vol. 65, no. 5, pp. 4331–4337, May 2018.

[13] J. Včelák, P. Ripka, and A. Zikmund, "Long-range magnetic tracking system," *IEEE Sensors J.*, vol. 15, no. 1, pp. 491–496, Jan. 2015.

[14] H. Wang, S. Y. Wang, H. B. Liu, K. Rhode, Z.-G. Hou, and R. Rajamani, "3-D electromagnetic position estimation system using high-magnetic-permeability metal for continuum medical robots," *IEEE Robot. Autom. Lett.*, vol. 7, no. 2, pp. 2581–2588, Apr. 2022.

[15] S. Song, H. Ren, and H. Yu, "An improved magnetic tracking method using rotating uniaxial coil with sparse points and closed form analytic solution," *IEEE Sensors J.*, vol. 14, no. 10, pp. 3585–3592, Oct. 2014.

[16] V. Pasku, A. De Angelis, G. De Angelis, A. Moschitta, and P. Carbone, "Magnetic field analysis for 3-D positioning applications," *IEEE Trans. Instrum. Meas.*, vol. 66, no. 5, pp. 935–943, May 2017.

[17] H. Dai, S. Song, X. Zeng, S. Su, M. Lin, and M.-Q. Meng, "6-D electromagnetic tracking approach using uniaxial transmitting coil and tri-axial magneto-resistive sensor," *IEEE Sensors J.*, vol. 18, no. 3, pp. 1178–1186, Feb. 2018.

[18] C. Vergne, C. Fery, T. Quirin, H. Nicolas, S. Madec, S. Hemm, and J. Pascal, "Low-field electromagnetic tracking using 3-D magnetometer for assisted surgery," *IEEE Trans. Magn.*, vol. 59, no. 2, pp. 1–5, Feb. 2023.

[19] D. Ambrus, M. Simic, D. Vasic, and V. Bilas, "Close-range electromagnetic tracking of pulse induction search coils for subsurface sensing," *IEEE Trans. Instrum. Meas.*, vol. 70, pp. 1–13, 2021.

[20] M. Cavaliere, O. McVeigh, H. A. Jaeger, S. Hinds, K. O'Donoghue, and P. Cantillon-Murphy, "Inductive sensor design for electromagnetic tracking in image guided interventions," *IEEE Sensors J.*, vol. 20, no. 15, pp. 8623–8630, Aug. 2020.

[21] J. B. Hummel, M. R. Bax, M. L. Figl, Y. Kang, C. Maurer, W. W. Birkfellner, H. Bergmann, and R. Shahidi, "Design and application of an assessment protocol for electromagnetic tracking systems," *Med. Phys.*, vol. 32, no. 7, pp. 2371–2379, 2005.

[22] A. Plotkin and E. Paperno, "3-D magnetic tracking of a single subminiature coil with a large 2-D array of uniaxial transmitters," *IEEE Trans. Magn.*, vol. 39, no. 5, pp. 3295–3297, Sep. 2003.

[23] K. M. Lee and H. Son, "Distributed multipole model for design of permanent-magnet-based actuators," *IEEE Trans. Magn.*, vol. 43, no. 10, pp. 3904–3913, Oct. 2007.

[24] J. Jeon, W. Chung, and H. Son, "Magnetic induction tomography using magnetic dipole and lumped parameter model," *IEEE Access*, vol. 7, pp. 70287–70295, 2019.

CHUN-YEON LIN (Member, IEEE) received the B.S. degree in mechanical engineering from National Central University, Taoyuan, Taiwan, in 2003, the M.S. degree in electrical control engineering from National Yang Ming Chiao Tung University, Hsinchu, Taiwan, in 2005, the M.S. degree in mechanical engineering from Stanford University, Stanford, CA, USA, in 2011, and the Ph.D. degree in mechanical engineering from the Georgia Institute of Technology, Atlanta, GA, USA, in 2017.

He is currently an Assistant Professor with the Department of Mechanical Engineering, National Taiwan University, Taipei, Taiwan. His current research interests include mechatronics, sensors, robotics, and system dynamics and control.

YI-CHIN WU (Graduate Student Member, IEEE) received the B.S. degree in mechanical engineering from National Cheng Kung University, Tainan, Taiwan, in 2019, and the M.S. degree in mechanical engineering from National Taiwan University, Taipei, Taiwan, in 2021, where he is currently pursuing the Ph.D. degree in mechanical engineering. His research interests include mechatronics and electromagnetic systems.

ZHONG-HSIANG KUO received the B.S. degree in mechanical engineering from the National Taiwan University of Science and Technology, Taipei, Taiwan, in 2021. He is currently pursuing the M.S. degree in mechanical engineering with National Taiwan University, Taipei. His research interests include mechatronics and electromagnetic systems.

HSI-YEN MA received the B.S. degree in mechanical engineering from National Yang Ming Chiao Tung University, Hsinchu, Taiwan, in 2019, and the M.S. degree in mechanical engineering from National Taiwan University, Taipei, Taiwan, in 2022. His research interest includes electromagnetic systems.

MEGAN TENG received the B.S. degree in mechanical engineering and the B.B.A. degree in international business from National Taiwan University, Taipei, Taiwan, in 2021. She is currently pursuing the Ph.D. degree in mechanical engineering with the University of California, Berkeley, CA, USA. She was a Research Assistant at the Department of Mechanical Engineering, National Taiwan University, from 2021 to 2022. Her current research interests include mechatronics and electromagnetic systems.

● ● ●